

## Article

**Nanoporous Silicon-Assisted Patterning of Monolayer MoS with Thermally Controlled Porosity: A Scalable Method for Diverse Applications**

Grace G. D. Han, Brendan D. Smith, Wenshuo Xu, Jamie H. Warner, and Jeffrey C. Grossman

ACS Appl. Nano Mater., **Just Accepted Manuscript** • DOI: 10.1021/acsanm.8b00707 • Publication Date (Web): 06 Jun 2018Downloaded from <http://pubs.acs.org> on June 12, 2018**Just Accepted**

“Just Accepted” manuscripts have been peer-reviewed and accepted for publication. They are posted online prior to technical editing, formatting for publication and author proofing. The American Chemical Society provides “Just Accepted” as a service to the research community to expedite the dissemination of scientific material as soon as possible after acceptance. “Just Accepted” manuscripts appear in full in PDF format accompanied by an HTML abstract. “Just Accepted” manuscripts have been fully peer reviewed, but should not be considered the official version of record. They are citable by the Digital Object Identifier (DOI®). “Just Accepted” is an optional service offered to authors. Therefore, the “Just Accepted” Web site may not include all articles that will be published in the journal. After a manuscript is technically edited and formatted, it will be removed from the “Just Accepted” Web site and published as an ASAP article. Note that technical editing may introduce minor changes to the manuscript text and/or graphics which could affect content, and all legal disclaimers and ethical guidelines that apply to the journal pertain. ACS cannot be held responsible for errors or consequences arising from the use of information contained in these “Just Accepted” manuscripts.

# Nanoporous Silicon-Assisted Patterning of Monolayer MoS<sub>2</sub> with Thermally Controlled Porosity: A Scalable Method for Diverse Applications

*Grace G. D. Han<sup>1†</sup>, Brendan D. Smith<sup>1†</sup>, Wenshuo Xu<sup>2</sup>, Jamie H. Warner<sup>2</sup>, Jeffrey C. Grossman<sup>1\*</sup>*

<sup>1</sup>Department of Materials Science and Engineering, Massachusetts Institute of Technology, 77  
Massachusetts Avenue, Cambridge, MA, 02139, USA.

<sup>2</sup>Department of Materials, University of Oxford, 16 Parks Road, Oxford, OX1 3PH, United  
Kingdom

Email: [jcg@mit.edu](mailto:jcg@mit.edu)

<sup>†</sup>Equal contributions

## Abstract

**Nanoscale pore formation on chemical vapor deposition grown monolayer MoS<sub>2</sub> is achieved using oxygen plasma etching through a nanoporous silicon mask, creating round pores of ~70 nm in diameter. The microscale areas with high porosity were successfully patterned via the usage of silicon masks. Thermal annealing in air after the pore formation in the monolayers results in the gradual enlargement of the pores, providing an effective method of controlling edge-to-area ratio of MoS<sub>2</sub> crystals. The photoluminescence of the**

1  
2  
3  
4 **nanoporous MoS<sub>2</sub> exhibits rapid increase and blue-shift due to facile p-doping during the**  
5 **thermal annealing process, compared to pristine MoS<sub>2</sub>. This method of fabricating porous**  
6 **transition metal dichalcogenide layers with controlled edge densities presents opportunities**  
7 **in various applications that require atomically thin nano-materials with controlled pore**  
8 **density and edge sites, such as filtration, electrocatalysis, and sensing.**  
9  
10  
11  
12  
13  
14  
15  
16  
17

18 **Keywords: Molybdenum disulfide, two-dimensional materials, nanoporous silicon,**  
19 **patterning, oxygen plasma, porosity, thermal annealing, catalysis**  
20  
21  
22

23  
24 Two-dimensional (2D) nanoporous materials, due to their atomically thin structures and  
25 mechanical strength, are being explored as an alternative class of materials for many applications,  
26 including sensors,<sup>1</sup> catalysts,<sup>2</sup> filtration membranes,<sup>3,4</sup> and electronic devices.<sup>5</sup> In all of these  
27 cases, precise control over porosity, pore size, and pore location is crucial in order to obtain the  
28 desirable mechanical, thermal, electrical, and transport properties necessary to advance these  
29 devices in their respective fields.  
30  
31  
32  
33  
34  
35  
36  
37

38 The challenges of constructing precise nanopores or a narrow range of pore dimensions,  
39 particularly over large areas, make the application of 2D nanoporous materials for commercial  
40 use difficult, along with the complicated fabrication of large-scale defect-free monolayers.  
41  
42 Generating selective nanoporous regions on 2D materials, which enables the localization of  
43 active area and protection of the rest of surface in sensors and other electronic devices, has been  
44 also challenging and time-consuming. Reported methods for nanopore generation range from ion  
45 bombardment and oxidation,<sup>6</sup> which rely on the naturally occurring defects, to precise drilling  
46 techniques involving focused ion beam<sup>7</sup> or electron beam<sup>8</sup> that require longer fabrication time  
47  
48  
49  
50  
51  
52  
53  
54  
55  
56  
57  
58  
59  
60

1  
2  
3  
4 and are limited to small-scale substrates. For larger-scale and more rapid nano-patterning, block  
5  
6 copolymer (BCP) lithography has been conducted on graphene<sup>9</sup> and MoS<sub>2</sub>,<sup>10</sup> showing the large-  
7  
8 scale generation of the ordered arrays of nano-features including nanodots, nanorods, and  
9  
10 hexagonal nanomesh of 15-20 nm dimensions. The nanomesh created by the BCP lithography  
11  
12 can be a potential nanoporous membrane material that is generated by the simple and fast nano-  
13  
14 patterning technique, despite the current state-of-the-art patterning capability restricted to a few  
15  
16 micron scale due to the non-uniform BCP phase separation across the cm-size substrates<sup>10</sup> or  
17  
18 limited by the micron scale substrate.<sup>9</sup>  
19  
20  
21  
22

23  
24 While the optimization of the BCP lithography technique will enable the fabrication of  
25  
26 uniform nanomeshes of TMD monolayers, alternative lithographic methods utilizing non-  
27  
28 polymeric mask materials have also been explored, including nanoporous anodized aluminum  
29  
30 oxide (AAO) which has been applied to graphene<sup>11</sup> and MoS<sub>2</sub><sup>12</sup> patterning. Such an approach  
31  
32 offers advantages with regard to its highly controllable pore sizes, ordered structures, and  
33  
34 physical and chemical durability during the etch process. There also exist drawbacks associated  
35  
36 with the implementation of this mask material, however, namely the fragility and high cost of  
37  
38 AAO which limit its scalability, and in general the lack of mask resolution at the sub-30 nm scale  
39  
40 demonstrated to this point for any such approach. In order to further leverage the favorable  
41  
42 properties of such nanoporous masks, the development of robust and finely tunable materials  
43  
44 with improved feature sizes must be further advanced.  
45  
46  
47  
48

49  
50 Here we explore the use of nanoporous silicon (NPSi) membranes as mask materials for  
51  
52 the patterning of MoS<sub>2</sub> via oxygen plasma etching. NPSi is a widely studied material spanning  
53  
54 multiple fields, but to the best of our knowledge has yet to be utilized as a mask for the  
55  
56  
57  
58  
59  
60

1  
2  
3  
4 patterning of 2D materials. This is likely due to the lack of available processes which can  
5  
6 produce sufficiently small (sub-30 nm) pores in silicon with aspect ratios greater than 10:1, in  
7  
8 order to penetrate sufficiently thick freestanding films so as to provide mechanical stability over  
9  
10 large areas. Previous ground-breaking work on the production of NPSi membranes by Fissell *et*  
11  
12 *al*<sup>13</sup> and Gaborski *et al*<sup>14</sup> resulted in pore diameters below 30 nm, but is limited to membrane  
13  
14 sizes on the order of mm<sup>2</sup> or less, which is a precluding factor for the large-area processing of 2D  
15  
16 materials. By leveraging a novel approach for the production of porous silicon membranes,  
17  
18 containing nanopores with aspect ratios greater than 1000:1 and diameters less than 20 nm, we  
19  
20 demonstrate the direct applicability of NPSi as an etch mask for the patterning of MoS<sub>2</sub>, and 2D  
21  
22 materials in general over arbitrarily large areas. Particularly we demonstrate the patterning of  
23  
24 areas with porosity, which is realized by the use of silicon masks where nanoporous areas are  
25  
26 confined to micron scale. Upon the generation of nanoporous 2D monolayers, the pore size is  
27  
28 further controlled by facile thermal annealing in air, which was monitored by optical  
29  
30 spectroscopy and electron microscopy.  
31  
32  
33  
34  
35

## 36 37 **Results and Discussion**

### 38 39 40 **Fabrication of nanoporous silicon (NPSi) masks and their morphology dependence on** 41 42 **substrate thickness.** 43 44

45  
46 Robust large-area NPSi membrane masks were fabricated for the first time via a modified  
47  
48 technique which was previously used for generating a partially nanoporous silicon substrate with  
49  
50 high aspect ratio dead-end pores.<sup>15</sup> In brief, silver films of 1 angstrom nominal thickness were  
51  
52 sputtered onto a (100) Si surface, resulting in the nucleation of hemispherical nanoislands.  
53  
54 Samples were then submerged in a solution of hydrogen peroxide and hydrofluoric acid (HF) for  
55  
56  
57  
58  
59  
60

1  
2  
3  
4 varying amounts of time, facilitating the etching of nanopores via a process known as metal-  
5 assisted chemical etching (MACE),<sup>16</sup> whereby oxidation occurs locally at the silicon-catalyst  
6 interface, and oxide is subsequently consumed by HF. This electroless etching process is only  
7 limited by the presence of reactants in solution, and when performed over extended periods of  
8 time can produce pores of aspect ratio over 1000:1 which completely penetrate Si substrates  
9 many microns in thickness.  
10  
11

12  
13  
14  
15  
16  
17  
18 Two types of mask were explored in this work. The first is a 50 nm-thick (100) NPSi  
19 layer, etched for 1-2 min following catalyst deposition (Figure 1(a) to 1(c)), and the second is an  
20 approximately 15  $\mu\text{m}$ -thick (100) NPSi layer, etched for 24 hours (Figure 1(d) to 1(f)). While the  
21 50 nm-thick mask allows for pore diameters less than 10 nm after 1 min etching (Figure 1(c)) or  
22  $\sim 15$  nm upon 2 min etching, it is fragile, and therefore only available as a free-standing film in  
23 100  $\mu\text{m}$  by 100  $\mu\text{m}$  windows. In contrast, the 15  $\mu\text{m}$ -thick mask may be produced over many  
24  $\text{cm}^2$  of area, but has a larger average pore diameter of 13.5 nm as indicated by Brunauer–  
25 Emmett–Teller (BET) nitrogen desorption analysis (Figure S1). Part of the pore size increase in  
26 the thick mask as measured by BET can be attributed to the heavily roughened surface and the  
27 underlying few micrometers of highly perforated material (Figure 1(e)), though imaging of the  
28 smoother back surface in contact with the  $\text{MoS}_2$  during patterning (Figure 1(f)) also reveals  
29 larger pore diameters than are present in the thin masks. For the 50 nm-thick masks, transmission  
30 electron microscopy (TEM) imaging of thousands of pores suggests an areal porosity of  
31 approximately 2.8% (Figure 1(c)) at the surface where etching is initiated. In the case of the thin  
32 NPSi masks, it is reasonable to assume that the majority of pores penetrate through the film  
33 completely, given that etching is observed to proceed at a rate greater than 65 nm/min to depths  
34 greater than 4  $\mu\text{m}$  in bulk Si, where etching would be expected to experience significant  
35  
36  
37  
38  
39  
40  
41  
42  
43  
44  
45  
46  
47  
48  
49  
50  
51  
52  
53  
54  
55  
56  
57  
58  
59  
60

retardation given the increased difficulty of reactant diffusion into the ultrahigh aspect ratio pores. These observations facilitate an estimate of 1-2% for areal porosity on the opposite side of the 50 nm-thick NPSi masks. In the context of masking materials, it is areal porosity which will play a dominant role in governing the extent to which the underlying material will be exposed to plasma etching, and specifically the areal porosity of the mask at the NPSi-MoS<sub>2</sub> interface.

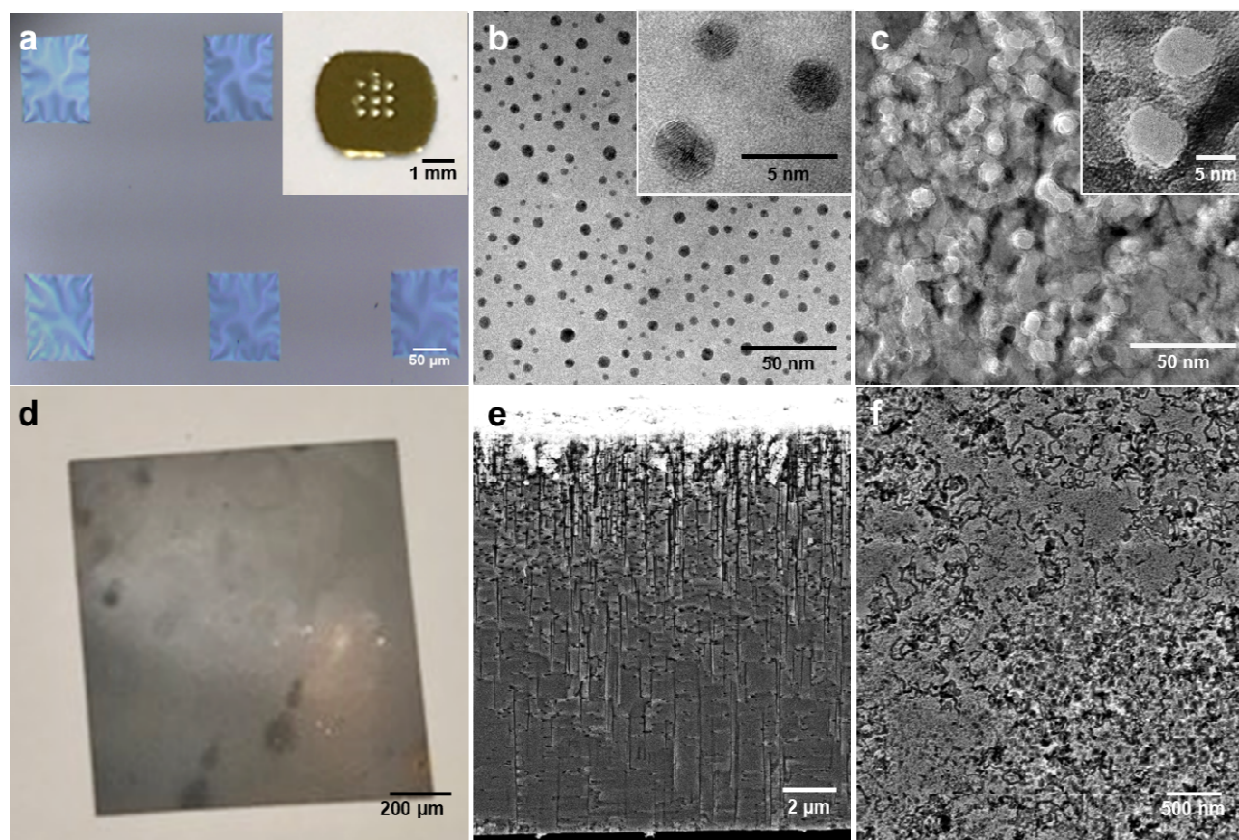


**Figure 1.** (a) Optical microscope image of five crystalline Si (c-Si) windows (100  $\mu\text{m}$  by 100  $\mu\text{m}$ ) of 50 nm thickness on a single silicon mask chip (3 mm by 3 mm). The patterned mask defines the areas to be porous after etching. (inset: a photograph of an entire silicon mask chip containing ten 50 nm-thick c-Si windows). (b) TEM image of a 50 nm-thick c-Si window coated with Ag nanoisland catalysts via radio frequency (RF) sputtering. (c) TEM image of a porous 50

1  
2  
3  
4 nm-thick c-Si window following 1 min of MACE (inset: sub-10 nm pores in the NPSi layer  
5  
6 etched via the MACE process). (d) Photograph of a  $\sim 1 \text{ cm}^2$  NPSi mask of 15  $\mu\text{m}$  thickness. (e)  
7  
8 SEM cross-sectional image of the 15  $\mu\text{m}$ -thick NPSi mask in (d). Porosity is observed to  
9  
10 decrease with depth due to the lack of completely anisotropic etching in the MACE process. (f)  
11  
12 SEM image of the bottom surface of the NPSi mask in (e), which is the surface in contact with  
13  
14 the  $\text{MoS}_2$  flakes during oxygen plasma exposure.  
15  
16  
17  
18

### 19 **Patterning process of monolayer $\text{MoS}_2$ using NPSi masks.**

20  
21  
22 A schematic illustration of the patterning process is shown in Figure 2(a). The chemical vapor  
23  
24 deposition (CVD)-grown  $\text{MoS}_2$  domains (10–100  $\mu\text{m}$ ) on silicon wafer with a 300 nm silicon  
25  
26 oxide layer were spin-coated with poly(methyl methacrylate) (PMMA) and transferred onto a  
27  
28 NPSi substrate via KOH-assisted etching of the silicon oxide layer. The substrate was exposed to  
29  
30  $\text{O}_2$  plasma selectively on the opposite side of  $\text{MoS}_2/\text{PMMA}$ , in order to etch only the nanoscale  
31  
32 fractional areas of  $\text{MoS}_2$  that are in contact with the nanopore areas of the NPSi mask. Then the  
33  
34 NPSi mask was removed by KOH-assisted etching, and the  $\text{MoS}_2/\text{PMMA}$  layer was transferred  
35  
36 to another silicon wafer. After the removal of PMMA coating by acetone, the nanoporous  $\text{MoS}_2$   
37  
38 domains were examined by optical microscopy, scanning electron microscopy (SEM), and  
39  
40 photoluminescence (PL) and Raman spectroscopy. The initial porous structures were then further  
41  
42 modified by thermal annealing in air, while the structural changes were investigated by the  
43  
44 microscopy and spectroscopy tools.  
45  
46  
47  
48  
49

50  
51 Imaging of the  $\text{MoS}_2$  domains following oxygen plasma exposure through the NPSi mask  
52  
53 reveals the introduction of significant porosity in the material. This is exemplified via  
54  
55 comparison between pristine  $\text{MoS}_2$  domains (Figure 2(b) and 2(c)) and those patterned by  
56  
57  
58  
59  
60

1  
2  
3  
4 selective etching through a thin (50 nm) NPSi mask (Figure 2(d) to 2(g)), where the latter  
5  
6 possesses an average porosity of 8.5%, with a pore diameter of  $65.9 \pm 13.3$  nm. The measured  
7  
8 porosity of 8.5% in the MoS<sub>2</sub> is nearly an order of magnitude greater than the estimated mask  
9  
10 porosity of 1-2% at the NPSi-MoS<sub>2</sub> interface, which is not unexpected given that the O<sub>2</sub> plasma  
11  
12 is capable of etching laterally once an initial defect is produced in the MoS<sub>2</sub> domains.  
13  
14  
15

16  
17 In addition to MoS<sub>2</sub>, a large family of 2D materials stand to benefit from the ability to  
18  
19 induce large-scale nanoporosity across initially pristine domains. The relevance of the developed  
20  
21 approach is evaluated by extension to the nano-patterning of tungsten disulfide (WS<sub>2</sub>). Figure  
22  
23 2(h) shows a WS<sub>2</sub> domain patterned with a 15 μm-thick NPSi mask (1 cm by 1 cm) over 4-5 μm  
24  
25 continuous area, and the magnified images (Figure 2(i) and 2(j)) indicate the morphology of the  
26  
27 nanoporous domain resembling that of the 15 μm-thick NPSi mask. The density and size of  
28  
29 pores generated by the large-scale free-standing mask is comparable to those observed in Figure  
30  
31 2(d) to 2(g), which indicates the scalability of this patterning method over a range of Si mask  
32  
33 thickness and lateral dimension. Given the successful patterning of WS<sub>2</sub> domains, we expect the  
34  
35 application of the etching technique to be extended to general sets of 2D materials including  
36  
37 graphene, *h*-BN, and other TMDs.  
38  
39  
40  
41

42  
43 We note that the O<sub>2</sub> plasma etching through NPSi masks completed in different time  
44  
45 scales depending on the thickness of the masks. The plasma treatment of 2 min was required to  
46  
47 pattern TMD domains through 50 nm-thick Si masks with sub-10 nm pores, while 30 sec  
48  
49 exposure to plasma through 15 μm-thick Si masks was sufficient to generate similar scale pores  
50  
51 on the domains. The shorter plasma treatments in each case resulted in the nanoporous domains  
52  
53  
54  
55  
56  
57  
58  
59  
60

with smaller pores which were difficult to distinguish from naturally occurring defects under SEM.

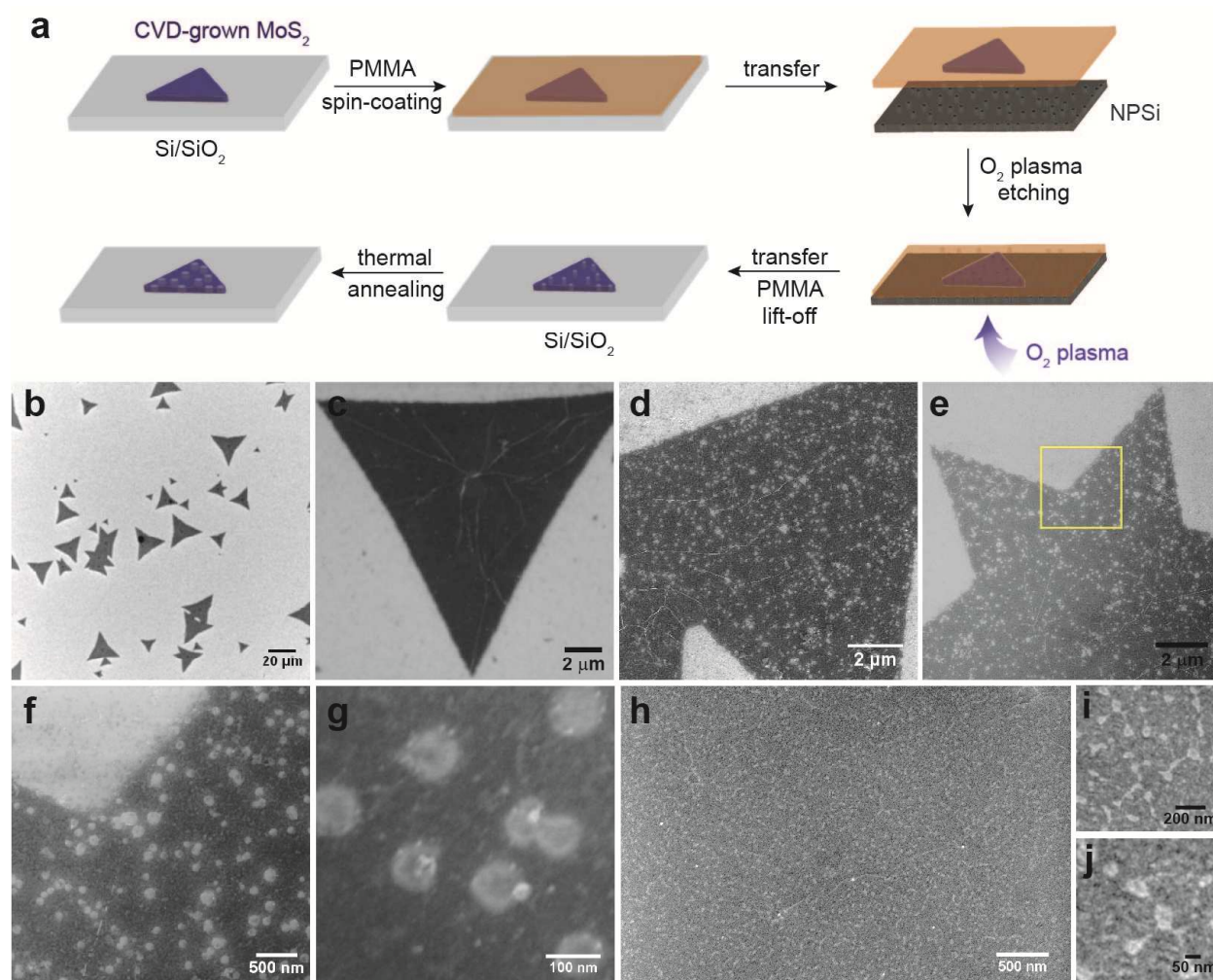


**Figure 2.** (a) Schematic illustration of the NPSi-assisted patterning process for nanoporous monolayer TMDs and the subsequent thermal annealing process to control the porosity. (b) SEM image of pristine MoS<sub>2</sub> domains on a Si/SiO<sub>2</sub> substrate. (c) SEM image of a single triangular MoS<sub>2</sub> domain that underwent the patterning process without being exposed to O<sub>2</sub> plasma as covered by the silicon mask chip. (d) SEM image of a nanoporous MoS<sub>2</sub> domain produced via selective etching through a thin (50 nm) NPSi mask for 2 min. (e) SEM image of a star-shaped

1  
2  
3  
4 nanoporous MoS<sub>2</sub> domain that is found on the identical substrate as (d). (f) Magnified view of  
5  
6 the region indicated with the yellow box in (e) showing the nanoscale pores with a range of  
7  
8 diameters. (g) High magnification SEM image of a nanoporous MoS<sub>2</sub> domain. (h) SEM image of  
9  
10 a nanoporous WS<sub>2</sub> domain following 30 sec of O<sub>2</sub> plasma etching using a 1 cm<sup>2</sup> NPSi mask of 15  
11  
12 μm thickness. (i) Magnified view of the sample in (h) showing less round and connected  
13  
14 morphology of nanopores on WS<sub>2</sub> domains. (j) Magnified view of the sample in (h) showing the  
15  
16 comparable size of pores to those in (g).  
17  
18  
19  
20  
21  
22

### 23 **Porosity of monolayer MoS<sub>2</sub> controlled by post-patterning thermal annealing process.**

24  
25  
26

27 Following initial O<sub>2</sub> plasma treatment of 2 min which generates round pores as determined by  
28  
29 the shape of the NPSi structures, an effective strategy to control the pore size of monolayer MoS<sub>2</sub>  
30  
31 domains was demonstrated via thermal treatment at 300 °C in air. Defect sites of MoS<sub>2</sub> flakes are  
32  
33 prone to oxidative etching under high temperature conditions,<sup>17,18</sup> so we expect to control the  
34  
35 size of nanopores by gradual thermal annealing. The nanopore size and density increases with  
36  
37 heating time, indicating mass loss occurs from the edge of existing nanopores, most likely in the  
38  
39 form of S depletion. The enlargement of these holes results in an increased edge to area ratio in  
40  
41 the MoS<sub>2</sub> sample. The increase of edge sites, which have implications in the optical and catalytic  
42  
43 properties, can be effectively modified by the simple heating process without the need of a  
44  
45 furnace or inert conditions. Depending on the application, the optimal edge-to-area ratio can be  
46  
47 selected, and diverse nanoscale patterns can be achieved.  
48  
49  
50  
51  
52

53 Until 30 min annealing, the oxidation does not lead to any visible change on the  
54  
55 morphology of the nano-pattern under SEM. Figures 3(a) to 3(h) display the effect of annealing  
56  
57  
58  
59  
60

(30, 60, and 100 min), which is the expansion of pores and their convergence due to the oxidation of the edge sites of patterned MoS<sub>2</sub>. The product of oxidation, MoO<sub>3</sub> particles,<sup>19</sup> is visible in the magnified images as bright dots (Figure 3(h)). Figure 3(i) summarizes the effect of thermal annealing on the edge density and porosity of the MoS<sub>2</sub> domains following plasma treatment, where edge density is calculated via SEM image analysis in ImageJ (Figure S2). Unsurprisingly, porosity increases monotonically with annealing time, gradually over the first 30 min, then more aggressively, reaching  $87.3 \pm 2.6\%$  after 100 min at 300°C. Less intuitive is the effect of annealing time on edge density, a relationship for which a rigorous understanding could prove beneficial in catalytic and sensing-focused applications. Perhaps counterintuitively, edge density is observed to remain statistically similar after 30 min of annealing time. This can be explained by the convergence of pores as they expand, resulting in the decrease in edge-to-area ratio within the porous MoS<sub>2</sub> domain. This balancing effect is observed to dissipate however by 60 min of annealing, primarily due to drastically increased pore intercalation corresponding with a significantly greater porosity of  $55.2 \pm 10.1\%$ , resulting in a near doubling of edge density from  $0.00827 \pm 0.00170 \text{ nm}^{-1}$  after 30 min to  $0.0145 \pm 0.00106 \text{ nm}^{-1}$ . Further annealing is observed to have a negative impact on edge density, as an increase in porosity to  $87.3 \pm 2.61\%$  after 100 min corresponds to a drop in edge density to  $0.0107 \pm 0.00135 \text{ nm}^{-1}$ , as connectivity between remaining MoS<sub>2</sub> regions is diminished. This result provides valuable insight for optimizing edge densities in MoS<sub>2</sub> and other 2D materials via nano-patterning and thermal annealing.

Figure 3(j) demonstrates the efficacy of the developed process, where half of a MoS<sub>2</sub> domain resting over a 50 nm thick NPSi porous mask region is nearly effectively patterned following O<sub>2</sub> plasma exposure, while the other half located on a non-porous region remains in a

1  
2  
3  
4 pristine state. This shows the seamless attachment of MoS<sub>2</sub> domains on the mask across the  
5  
6 boundary of the 50 nm-thick NPSi window and the supporting silicon chip, enabled by the  
7  
8 PMMA-assisted transfer and mild drying process at 100 °C. The SEM image showing the half-  
9  
10 patterned MoS<sub>2</sub> domain after 60 min of thermal annealing also confirms that the oxidation occurs  
11  
12 more extensively on the nanoporous side rather than on the pristine area under identical  
13  
14 annealing conditions. Figure 3(k) displays the formation of nanopores smaller than 50 nm in  
15  
16 diameter on a pristine MoS<sub>2</sub> domain after 100 min of thermal annealing in air, as previously seen  
17  
18 as triangular pits created by prolonged thermal annealing.<sup>19</sup> These pores formed in a lower  
19  
20 density than that of O<sub>2</sub> plasma etched pores are expected to grow via the preferential oxidation of  
21  
22 defect sites on the basal plane of MoS<sub>2</sub> and more severely around the domain edges and the  
23  
24 present cracks, as observed in SEM images (Figure S3).  
25  
26  
27  
28  
29

30 The understanding of the gradual morphology changes induced by thermal annealing  
31  
32 gives valuable insight for the optimization of porosity, which is essential for developing  
33  
34 porosity-dependent applications such as nanoporous filtration and edge-site-specific applications  
35  
36 including sensing and electrocatalysis.  
37  
38  
39  
40  
41  
42  
43  
44  
45  
46  
47  
48  
49  
50  
51  
52  
53  
54  
55  
56  
57  
58  
59  
60

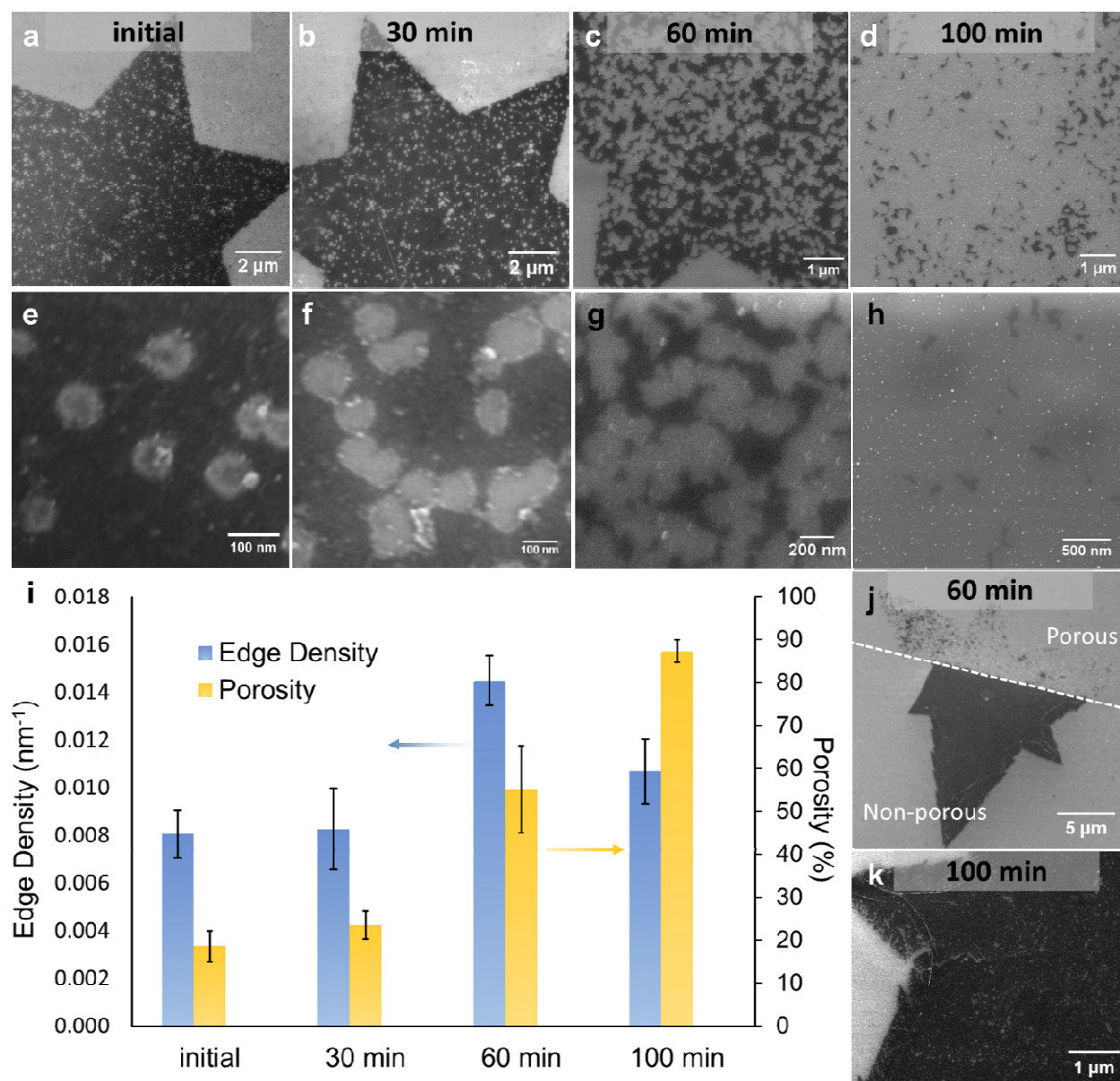


**Figure 3.** Effect of thermal annealing on the morphology of nanoporous  $\text{MoS}_2$ . (a) SEM image of a  $\text{MoS}_2$  domain after initial 2 min  $\text{O}_2$  plasma treatment through a 50 nm-thick NPSi mask. (b) SEM image of the  $\text{MoS}_2$  domain in (a) after 30 min of thermal annealing in air. (c) SEM image of a  $\text{MoS}_2$  domain from an identical sample after 60 min of annealing. (d) SEM image of a  $\text{MoS}_2$  domain from an identical sample after 100 min of annealing. (e) Magnified view of the sample in (a) showing individual pores with diameter  $\sim 70$  nm. (f) Magnified view of the sample in (b)

1  
2  
3  
4 showing nano-patterns of enlarged pores produced in the monolayer MoS<sub>2</sub>. (g) Magnified view  
5  
6 of the sample in (c) showing further expanded and converged pores. (h) Magnified view of the  
7  
8 sample in (d) showing MoS<sub>2</sub> flakes and oxidized MoS<sub>2</sub> particles. (i) Plot of MoS<sub>2</sub> edge density  
9  
10 and porosity with respect to thermal annealing time for O<sub>2</sub> plasma etched samples. N=3 for all  
11  
12 data. (j) SEM image of a MoS<sub>2</sub> domain located half on a 50 nm thick NPSi etch mask and half on  
13  
14 non-porous silicon after O<sub>2</sub> plasma treatment and 60 min of thermal annealing. (k) SEM image of  
15  
16 a pristine MoS<sub>2</sub> domain after 100 min of thermal annealing in air.  
17  
18  
19  
20  
21  
22  
23

### 24 **Optical properties of nanoporous MoS<sub>2</sub> with varied edge density.**

25  
26  
27 The visual changes of the domain morphology corroborate the optical property changes  
28  
29 measured by PL and Raman spectroscopy on the pristine and nanoporous MoS<sub>2</sub> (Figure 4).  
30  
31 Optical properties of MoS<sub>2</sub> samples were first measured by PL spectroscopy on the selected  
32  
33 spots of ~1 μm size within MoS<sub>2</sub> domains. Pristine MoS<sub>2</sub> domains before thermal annealing  
34  
35 exhibit PL spectra with a peak at 683 nm upon excitation at 514.5 nm (Figure 4(a)). As thermally  
36  
37 annealed at 300 °C, the PL increases and the peaks blue-shift to 680 nm after 40 min, 675 nm  
38  
39 after 60 min, and 660 nm after 100 min of heating. Prior work on block copolymer (BCP)-  
40  
41 assisted nano-patterned MoS<sub>2</sub> domains showed that increasing edge density causes PL  
42  
43 quenching,<sup>10</sup> which is different than the observations in this work. This is due to the differences  
44  
45 in edge density formation, where nanodots, nanorods, and nanomeshes in the prior work are not  
46  
47 subjected to oxidation at high temperature and were shown by ADF-STEM to have non-  
48  
49 reconstructed edges.  
50  
51  
52  
53  
54  
55  
56  
57  
58  
59  
60

1  
2  
3  
4 More remarkable PL increase and blue-shift are observed in the case of the nanoporous MoS<sub>2</sub>  
5 sample (Figure 4(b) and 4(c)). The O<sub>2</sub>-plasma etched domains exhibit PL spectra with a peak at  
6  
7 677 nm which blue-shifts to 664 nm after 20 min of thermal annealing at 300 °C. After the peak  
8  
9 shift, the PL intensity increases as the domains are heated up to 70 min, then further annealing  
10  
11 results in the quenching of PL due to severe degradation of the material. The PL change seen in  
12  
13 the nanoporous MoS<sub>2</sub> sample follows the trend of edge/area ratio (Figure 3(i)) as previously  
14  
15 determined by analyzing SEM images. It has been reported that laser induced chemisorbed  
16  
17 oxidation of CVD-grown pristine MoS<sub>2</sub> causes PL increase due to the reduction in n-doping  
18  
19 followed by PL decrease after continued oxidation,<sup>20</sup> and that heating exfoliated MoS<sub>2</sub> in air also  
20  
21 causes rapid PL enhancements.<sup>21</sup> Another report illustrates that defect areas or cracks on MoS<sub>2</sub>  
22  
23 layers exhibit a huge PL enhancement upon thermal annealing compared to pristine area due to  
24  
25 stronger binding to O<sub>2</sub>, which leads to more prominent p-doping, and less non-radiative  
26  
27 recombination around the defective sites.<sup>22</sup> A similar effect is seen in the nanoporous MoS<sub>2</sub>  
28  
29 samples as in Figure 4. The NPSi mask etched sample has more rapid PL increase compared to  
30  
31 the pristine MoS<sub>2</sub>, which is associated with the higher edge density and defectiveness in the  
32  
33 nanoporous domains as seen in Figures 2 and 3. For the MoS<sub>2</sub> sample that is not etched, only a  
34  
35 slight PL increase is observed within the same time frame of high temperature heating. The  
36  
37 immediate PL change of nanoporous MoS<sub>2</sub> upon brief thermal annealing is likely caused by  
38  
39 initial reduction of the n-doping level of MoS<sub>2</sub> through the physisorption of oxygen molecules.  
40  
41 The degradation of edge sites and the pore opening require further annealing (which may activate  
42  
43 chemisorption and molecular conversion) and are accelerated as the edge-to-area ratio increases.  
44  
45  
46  
47  
48  
49  
50  
51  
52  
53  
54  
55  
56  
57  
58  
59  
60

1  
2  
3  
4 Decoupling the contributions of exciton and trion emission to the PL spectra was  
5  
6 performed by multiple peak fitting in order to explain the overall blue-shift and PL changes as a  
7  
8 function of thermal annealing time. For pristine MoS<sub>2</sub>, which was not etched but transferred  
9  
10 multiple times during the nanopore fabrication process on the same substrate (Figure 2(a)), the  
11  
12 PL mostly consists of strong trion emission at ~1.83 eV, and the continued thermal annealing  
13  
14 induces exciton emission at ~1.87 eV. After 100 min annealing, the exciton/trion ratio was  
15  
16 calculated to be 0.3. The nanoporous MoS<sub>2</sub> exhibits similar behavior, as the exciton contribution  
17  
18 increases and dominates after thermal annealing. The trion emission observed at ~1.83 eV and  
19  
20 exciton at ~1.87 eV both grow rapidly following thermal oxidation, and the exciton/trion ratio  
21  
22 increases from 0.53 after 20 min to 1.07 after 50 min, 1.19 after 60 min, 1.32 after 70 min, and  
23  
24 1.43 after 80 min annealing (Figure S4). The exciton/trion ratio then drops to 0.77 after 100 min  
25  
26 thermal treatment. This analysis indicates that both nanoporous and non-porous samples are  
27  
28 heavily n-doped before thermal annealing as revealed by the initially dominating trion  
29  
30 contribution.<sup>23</sup> Both samples have a similar degree of surface residue, and the comparison of the  
31  
32 PL from both the etched and protected areas before the high temperature treatments shows  
33  
34 similar spectra (Figure S5) indicating that the doping and defect densities are similar in both  
35  
36 cases.  
37  
38  
39  
40  
41  
42  
43

44 Raman spectroscopy of both samples (Figure 4(d) and 4(e)) exhibit an unchanging A<sub>1g</sub>  
45  
46 mode and decreasing E<sup>1</sup><sub>2g</sub> mode with thermally annealing. The increasing A<sub>1g</sub>/E<sup>1</sup><sub>2g</sub> ratio indicates  
47  
48 doping level changes<sup>24</sup> occurring to the monolayer MoS<sub>2</sub> flakes upon thermal annealing,  
49  
50 consistent with the PL spectra changes. The negligible softening of the E<sup>1</sup><sub>2g</sub> mode suggests  
51  
52 insignificant changes in strain within the MoS<sub>2</sub> monolayers. Analysis of the time dependence of  
53  
54 the heating process (Figure 4(f)) shows an initial stage where minimal PL increase is observed,  
55  
56  
57  
58  
59  
60

which is likely due to a cleaning of surface residue, then a rapid onset of PL increase at 30-40 min (porous sample). The time scale of the rapid onset of PL is similar to prior studies on exfoliated MoS<sub>2</sub> materials,<sup>21</sup> where approximately 25 min at 300 °C causes the PL maxima to be reached, followed by a rapid PL quench during the next 25 min. The PL increase of pristine sample is much slower than that of nanoporous sample, which is associated with the larger surface area of pristine MoS<sub>2</sub> covered with amorphous carbon protecting layers and with the less available edge sites that are prone to oxidation process. The PL spectra were normalized to the Raman A<sub>1g</sub> peak, which normalizes the impact of different sample areas and materials quantity.<sup>25</sup>

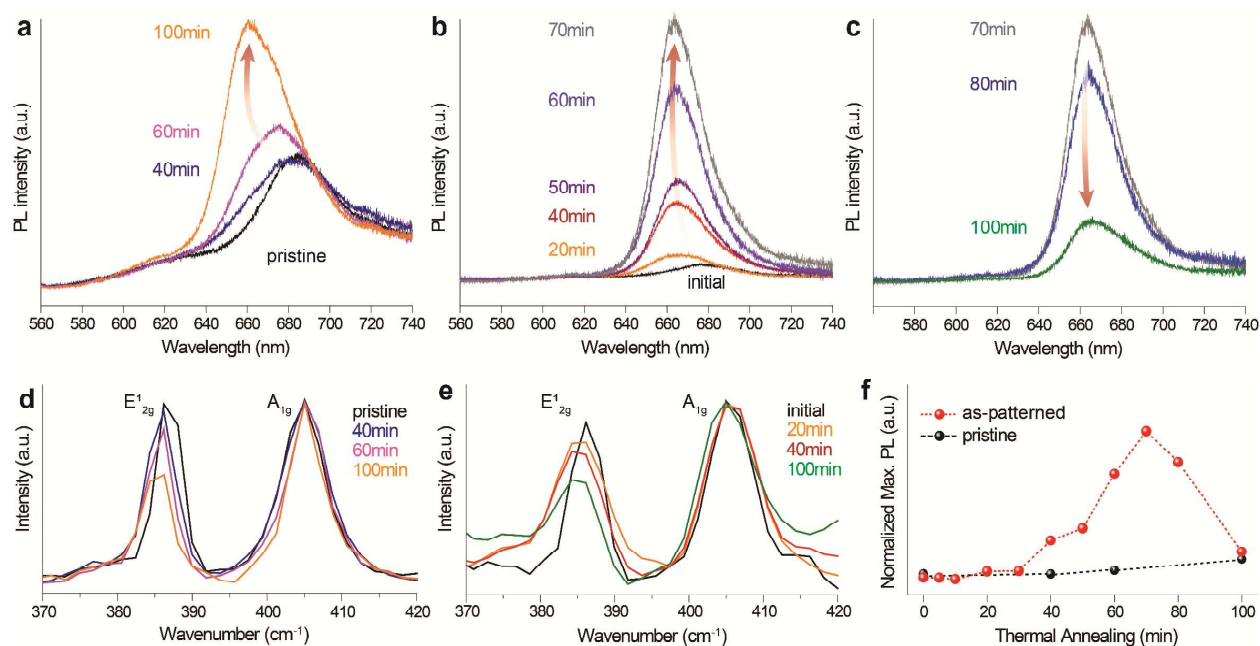


**Figure 4.** Optical property changes of MoS<sub>2</sub> domains induced by nano-patterning and thermal annealing. (a) Normalized photoluminescence (PL) spectra of pristine MoS<sub>2</sub> domains upon thermal annealing. (b) Normalized PL spectra of nanoporous MoS<sub>2</sub> domains upon thermal annealing up to 70 min. (c) Normalized PL spectra of nanoporous MoS<sub>2</sub> domains upon continued thermal annealing. (d) Normalized Raman spectra of pristine MoS<sub>2</sub> domains upon thermal

1  
2  
3  
4 annealing. (e) Normalized Raman spectra of nanoporous MoS<sub>2</sub> domains upon thermal annealing.  
5  
6 (f) Relative maximum PL intensity change as a function of annealing time for nano-patterned  
7  
8 and pristine MoS<sub>2</sub> domains. All spectra were normalized to the A<sub>1g</sub> signal intensity for each  
9  
10 sample.  
11  
12  
13  
14  
15

### 16 **Comparison to direct O<sub>2</sub> plasma exposure to MoS<sub>2</sub> without NPSi masks**

17  
18  
19 The active selective masking behavior of the fabricated NPSi layers was confirmed via  
20 control experiments in which CVD-grown pristine MoS<sub>2</sub> domains were directly exposed to O<sub>2</sub>  
21 plasma for short (1 sec, 10 sec, and 30 sec) times with no masking. Drastically different results  
22 were achieved, helping to elucidate the crucial role of the NPSi masks in patterning. After only 1  
23 sec of plasma exposure, the PL decreases and blue-shifts from 678 nm to 663 nm (Figure 5(a)), a  
24 phenomenon which was not observed in the plasma etching process through NPSi masks (Figure  
25 S5). Based on the Raman spectra in Figure 5(b), we can monitor the impact of p-doping on  
26 pristine MoS<sub>2</sub> upon the short plasma treatment. Any treatment longer than 1 sec destroys the  
27 material, resulting in the absence of PL or Raman signal from the samples.  
28  
29  
30  
31  
32  
33  
34  
35  
36  
37  
38  
39  
40

41 The morphology changes upon the direct plasma treatment were investigated by SEM  
42 (Figure 5 (c) to 5(h)). After 1 sec exposure to O<sub>2</sub> plasma, the domains exhibit homogeneous  
43 cracking across the materials without significant changes of nanoscale morphology such as pore  
44 formation or defect enlargement. The longer treatment generates domains with lighter contrast  
45 and bright needle-shaped materials of tens and hundreds of nm in length. The conversion of  
46 MoS<sub>2</sub> to the oxidation product is responsible for the annihilated PL and Raman signals. The  
47 detailed progress of cracking by the direct O<sub>2</sub> plasma treatment was investigated previously,  
48  
49  
50  
51  
52  
53  
54  
55  
56  
57  
58  
59  
60

1  
2  
3  
4 which describes the initially isolated crack appearance on intrinsic defects of MoS<sub>2</sub> basal plane.  
5  
6 These initial cracks then propagate to form interconnected cracks which possess angle of around  
7  
8 120° between them. STEM images showed both Mo and S terminated exposed edges of cracks  
9  
10 with angle of around 120°. <sup>2</sup> The control experiment demonstrates the unique capability of NPSi  
11  
12 masks in the selective formation of nanopores on 2D materials that exhibit bright PL even after  
13  
14 the nano-patterning and extensive etching, allowing for the preservation of morphological and  
15  
16 optoelectronic properties, while increasing edge density as desired. The localized nanoscale  
17  
18 pores are believed to possess interesting atomic structures of edge sites, and the investigation on  
19  
20 the atomic resolution imaging of the nanoporous MoS<sub>2</sub> and on the impact of thermal annealing  
21  
22 will be explored in future work.  
23  
24  
25  
26  
27  
28  
29  
30  
31  
32  
33  
34  
35  
36  
37  
38  
39  
40  
41  
42  
43  
44  
45  
46  
47  
48  
49  
50  
51  
52  
53  
54  
55  
56  
57  
58  
59  
60

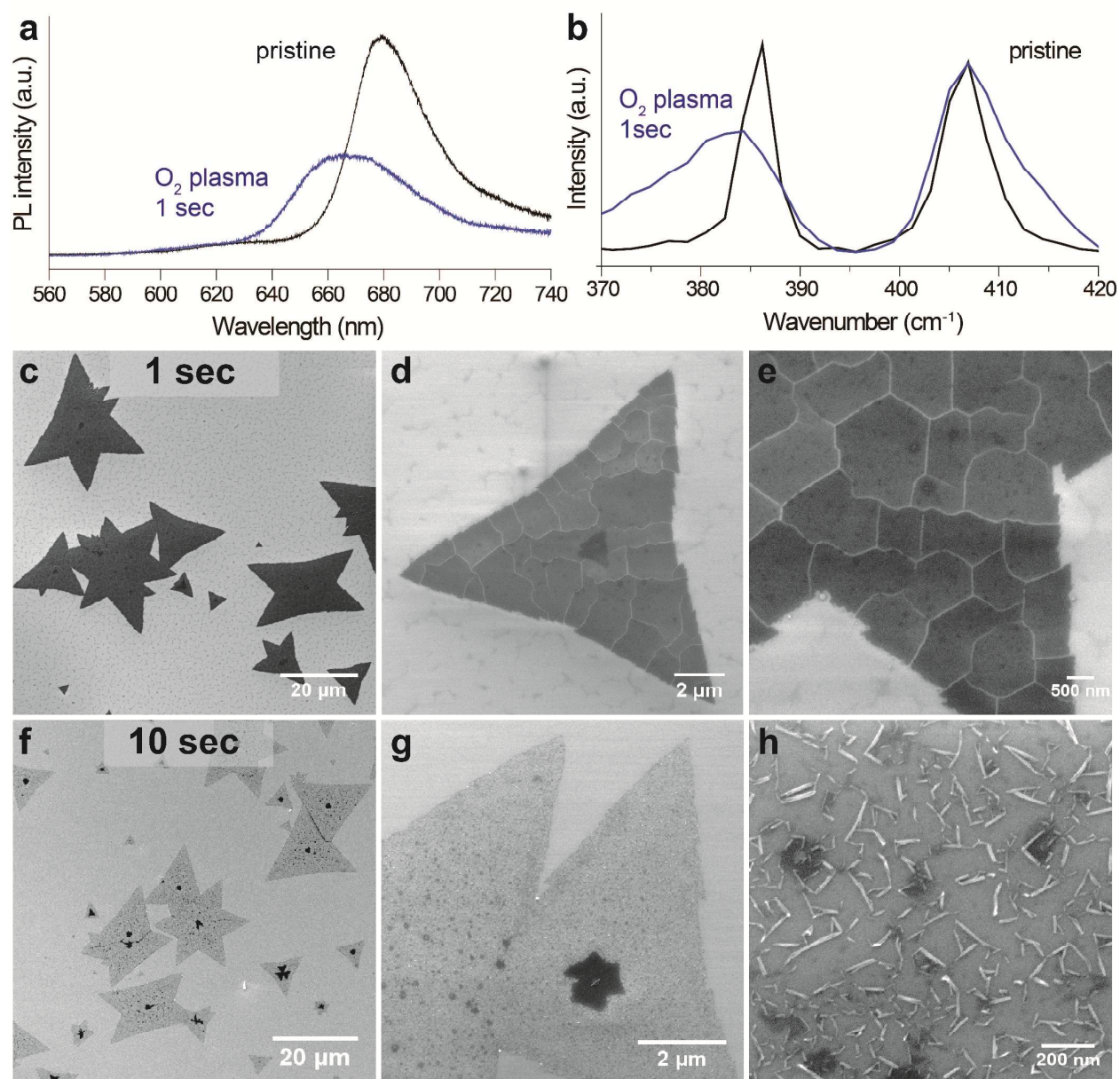


**Figure 5.** Optical property and morphology changes of MoS<sub>2</sub> domains induced by direct O<sub>2</sub> plasma exposure. (a) Normalized PL spectra of pristine MoS<sub>2</sub> domains before and after 1 sec direct O<sub>2</sub> plasma exposure. (b) Normalized Raman spectra of pristine MoS<sub>2</sub> domains before and after 1 sec direct O<sub>2</sub> plasma treatment. (c-e) SEM image of pristine MoS<sub>2</sub> domains after 1 sec direct O<sub>2</sub> plasma treatment with varied magnification. (f-h) SEM image of pristine MoS<sub>2</sub> domains after 10 sec direct O<sub>2</sub> plasma treatment with varied magnification.

## Conclusion

The newly developed nanoporous silicon membrane with a pore aspect ratio greater than 1000:1 and pore diameters less than 20 nm was used as an etch mask for 2D materials ( $\text{MoS}_2$  and  $\text{WS}_2$ ) nano-patterning. Application of the NPSi masks with lateral size ranging from 100  $\mu\text{m}$  by 100  $\mu\text{m}$  to 1 cm by 1 cm and thickness from 50 nm to 15  $\mu\text{m}$  was demonstrated, which revealed the scalability of the patterning method for 2D materials. The optimized process generated nanopores with diameters of  $\sim 70$  nm within the selected area of sample, and the successful enlargement of the pores was conducted by a simple thermal annealing step in air. Gradual changes of the pore size, edge-to-area ratio, and connectivity between the nano-flakes are fully correlated to optical property changes that indicate an increase of p-doping and exciton contribution as the nanoporous materials are mildly oxidized. This study opens opportunities towards optimizing the porosity and edge site density of 2D materials for various applications such as water filtration, sensing, and electrocatalysis. In the catalysis case, it is expected specifically that the greatly increased edge density will improve catalytic performance for the HER, as demonstrated in existing work.<sup>12</sup> Further, such a versatile patterning method could be applied to a range of materials beyond TMDs for large-scale applications.

## Methods.

### Chemical vapor deposition growth of monolayer $\text{MoS}_2$ .

Monolayer  $\text{MoS}_2$  was grown by CVD utilizing a smaller inner tube ( $\text{MoO}_3$ ) within a larger outer quartz tube (S).<sup>26</sup> This reduces the interaction between the S and  $\text{MoO}_3$  precursor during the growth. Molybdenum trioxide ( $\text{MoO}_3$ , powder,  $\geq 99.5\%$ , Sigma-Aldrich) and sulphur (S, powder,  $\geq 99.5\%$ , Sigma-Aldrich) are used as the precursors. The  $\text{MoO}_3$  (inner tube, 20 mg) and S (outer

1  
2  
3  
4 tube, 300 mg) were increased to  $\sim 180$  and  $\sim 300$  °C, respectively, while the 300 nm SiO<sub>2</sub>/Si  
5  
6 substrate positioned downstream was at  $\sim 800$  °C. This results in the CVD growth of MoS<sub>2</sub>  
7  
8 monolayer domains that range from 10-100  $\mu\text{m}$ . Sulphur vapour was flushed through the system  
9  
10 for 10 min before heating up the MoO<sub>3</sub>. When the final temperature for growth was achieved, the  
11  
12 MoS<sub>2</sub> nucleates under a 150 sccm argon flow for 17 min, and then the flow rate is reduced to 10  
13  
14 sccm for a 23-min growth. Finally, the reaction is stopped by moving the sample from hot zone  
15  
16 of the furnace and this gives fast cooling.  
17  
18  
19  
20

### 21 **Nanoporous silicon fabrication process.**

22  
23  
24 NPSi masks were fabricated from 50 nm thick (100) crystalline Si films (SiMPore Inc.) and 15  
25  
26  $\mu\text{m}$  thick (100) crystalline Si films, initially 300  $\mu\text{m}$  thick (100) DSP wafers, resistivity 1-10  
27  
28  $\Omega\cdot\text{cm}$ , p-type (boron doped), which were thinned via potassium hydroxide in 30 wt.% aqueous  
29  
30 solution at 70°C, as described in previous work.<sup>27</sup> Both types of substrate were cleaned in  
31  
32 acetone, isopropanol, and DI water, and dried under nitrogen prior to catalyst deposition. The  
33  
34 hemispherical nanocatalysts were deposited via RF magnetron sputtering using an ATC 6-target  
35  
36 sputtering tool (AJA International). In all experiments, Ag was deposited to a nominal thickness  
37  
38 of 1  $\square$  at an RF power of 30 W. Immediately after catalyst deposition, samples were submerged  
39  
40 in MACE solution containing 5.33 M HF and 0.12 M H<sub>2</sub>O<sub>2</sub> for 1 min in the case of the 50 nm  
41  
42 thick masks and 24 hours for the 15  $\mu\text{m}$  thick masks. Masks were rinsed extensively with DI  
43  
44 water upon completion of the etching and dried under nitrogen.  
45  
46  
47  
48  
49  
50  
51  
52  
53  
54  
55  
56  
57  
58  
59  
60

### **Nanoporous silicon masking and oxygen plasma etching process.**

On the substrate with CVD-grown monolayer MoS<sub>2</sub>, PMMA A7 solution was spin-coated (500 rpm for 5 sec, 2000 rpm for 10 sec, and 4500 rpm for 45 sec). The sample was annealed at 180 °C for 90 sec to evaporate anisole, and the Si/SiO<sub>2</sub> substrate was removed by dissolving in 1 M KOH solution overnight. The PMMA layer containing MoS<sub>2</sub> domains was then rinsed with DI water and transferred to NPSi substrate. The sample was dried at 150 °C for 10 min and turned upside-down to be selectively exposed to oxygen plasma. The oxygen plasma etching of MoS<sub>2</sub> through NPSi mask was conducted by using Harrick Scientific PDC-32G Plasma Cleaner (18 W, oxygen flow rate of 0.6 SCFH (standard cubic feet per hour)). The porous MoS<sub>2</sub> formed on PMMA layer was then transferred to a new Si/SiO<sub>2</sub> substrate via KOH etching of NPSi as described for the initial transfer process.

### **Measurements.**

PL and Raman spectra were acquired using a Horiba LabRAM 800 HR spectrometer equipped with an Ar<sup>+</sup> (514.5 nm) excitation source and a Peltier-cooled CCD detector. The laser was focused on the sample using a 100x objective under reflected illumination and the PL measured under confocal conditions with a 400 nm hole. The laser spot on the sample was ~1 μm in diameter and had a power of ~4 mW at the sample surface. Scanning electron microscopy was performed using Zeiss Ultra Plus FESEM.

**Data availability.** The data that support the findings of this study are available from the corresponding author upon request.

## Acknowledgements

The authors are grateful for the partial support from the Masdar Institute & MIT Cooperative Program. B.D.S. also receives support from the MIT Tata Center for Technology and Design, as well as the Natural Sciences and Engineering Research Council of Canada. This work was performed in part at the Harvard University Center for Nanoscale Systems (CNS), a member of the National Nanotechnology Coordinated Infrastructure Network (NNCI), which is supported by the National Science Foundation under NSF ECCS award no. 1541959. The authors also acknowledge the Center for Materials Science and Engineering (CMSE) at MIT for the use of the oxygen plasma generator. J.H.W. thanks the support from the Royal Society.

## Author contributions

G.G.D.H and B.D.S. conducted the patterning process of MoS<sub>2</sub> and characterized the morphology by SEM. G.G.D.H characterized optical properties of all samples. B.D.S. fabricated NPSi etch masks. W.X. provided CVD-grown MoS<sub>2</sub> samples. J.H.W. and J.C.G conceived and supervised the project. The manuscript was written through contributions of all authors. All authors have given approval to the final version of the manuscript.

## Notes

The authors declare no competing financial interest.

1  
2  
3  
4 **Supporting Information Available:** Supporting information includes BET characterization of  
5 porosity in the 15  $\mu\text{m}$  thick NPSi masks (Figure S1), details of image analysis for  $\text{MoS}_2$  porosity  
6 characterization (Figure S2), characterization of porosity in pristine  $\text{MoS}_2$  domains following  
7 annealing (Figure S3), optical characterization of nanoporous  $\text{MoS}_2$  following annealing (Figure  
8 S4), and optical characterization of pristine and nanoporous  $\text{MoS}_2$  prior to annealing (Figure S5).  
9  
10  
11  
12  
13  
14  
15  
16  
17  
18  
19

## 20 **References**

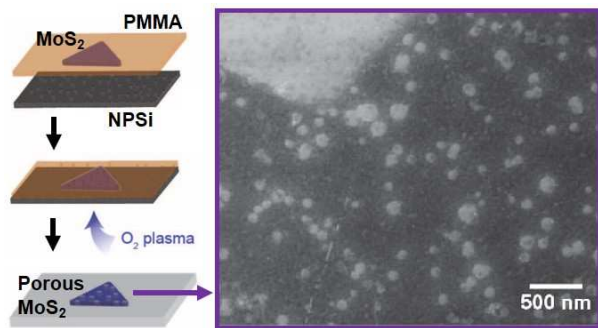
- 21  
22  
23 (1) Merchant, C. A.; Healy, K.; Wanunu, M.; Ray, V.; Peterman, N.; Bartel, J.; Fischbein, M.  
24 D.; Venta, K.; Luo, Z.; Charlie Johnson, A.T.; Drndic, M. DNA Translocation through  
25 Graphene Nanopores. *Nano Lett.* **2010**, *10*, 2915–2921.  
26  
27  
28  
29  
30  
31 (2) Ye, G.; Gong, Y.; Lin, J.; Li, B.; He, Y.; Pantelides, S. T.; Zhou, W.; Vajtai, R.; Ajayan, P.  
32 M. Defects Engineered Monolayer  $\text{MoS}_2$  for Improved Hydrogen Evolution Reaction.  
33 *Nano Lett.* **2016**, *16*, 1097–1103.  
34  
35  
36  
37  
38 (3) Jiang, D.; Cooper, V. R.; Dai, S. Porous Graphene as the Ultimate Membrane for Gas  
39 Separation. *Nano Lett.* **2009**, *9*, 4019–4024.  
40  
41  
42  
43 (4) Cohen-Tanugi, D.; Grossman, J. C. Water Desalination across Nanoporous Graphene.  
44 *Nano Lett.* **2012**, *12*, 3602–3608.  
45  
46  
47  
48 (5) Wang, H.; Sun, X.; Liu, Z.; Lei, Z. Creation of Nanopores on Graphene Planes with MgO  
49 Template for Preparing High-Performance Supercapacitor Electrodes. *Nanoscale* **2014**, *6*,  
50 6577–6584.  
51  
52  
53  
54  
55  
56  
57  
58  
59  
60

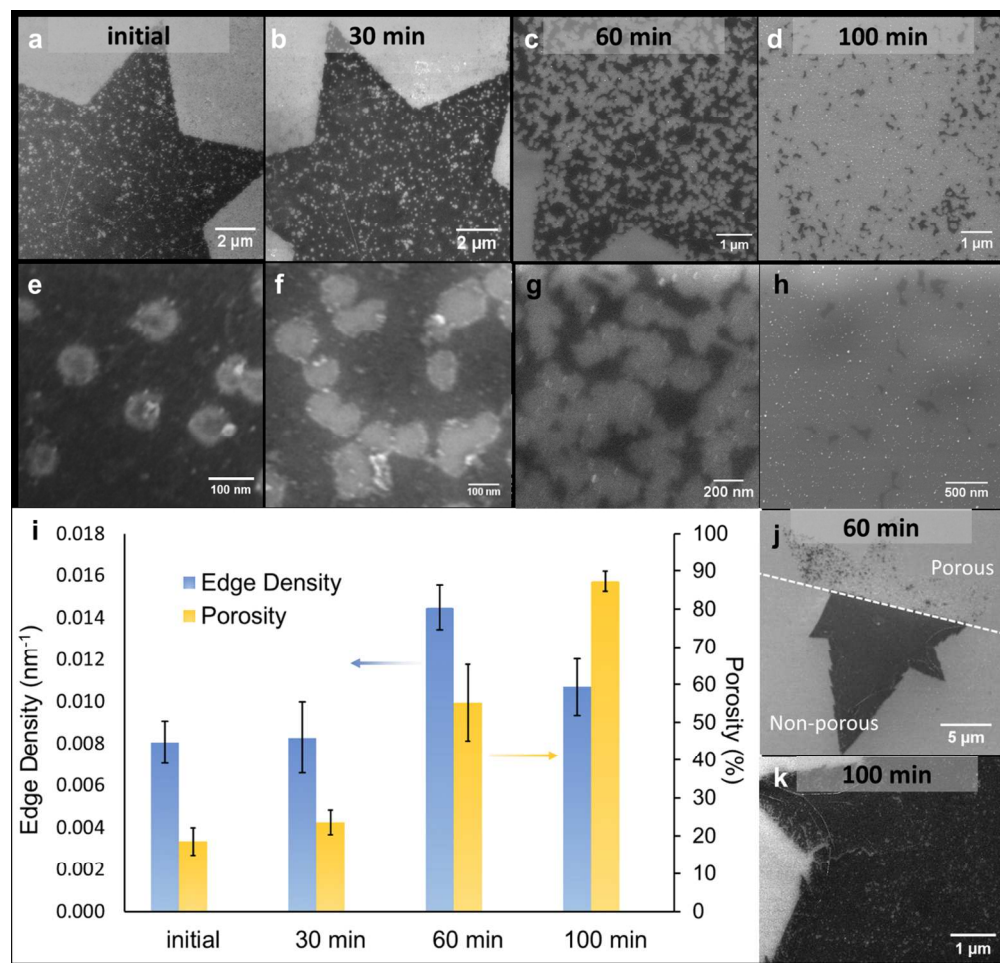
- 1  
2  
3  
4 (6) O'Hern, S. C.; Boutilier, M. S. H.; Idrobo, J. -C.; Song, Y.; Kong, J.; Laoui, T.; Atieh, M.;  
5 Karnik, R. Selective Ionic Transport through Tunable Sub-Nanometer Pores in Single-  
6 Layer Graphene Membranes. *Nano Lett.* **2014**, 140203110837009.  
7  
8  
9  
10  
11  
12 (7) Celebi, K.; Buchheim, J.; Wyss, R. M.; Droudian, A.; Gasser, P.; Shorubalko, I.; Kye, J. -  
13 I.; Lee, C.; Park, H. G. Ultimate Permeation Across Atomically Thin Porous Graphene.  
14 *Science* **2014**, 334, 289–293.  
15  
16  
17  
18  
19 (8) Fischbein, M. D.; Drndić, M. Electron Beam Nanosculpting of Suspended Graphene  
20 Sheets. *Appl. Phys. Lett.* **2008**, 93, 113107.  
21  
22  
23  
24  
25 (9) Bai, J.; Zhong, X.; Jiang, S.; Huang, Y.; Duan, X. Graphene Nanomesh. *Nat. Nanotechnol.*  
26 **2010**, 5, 190–194.  
27  
28  
29  
30 (10) Han, G. G. D.; Tu, K. -H.; Niroui, F.; Xu, W.; Zhou, S.; Wang, X.; Bulovic V.; Ross, C.  
31 A.; Warner, J. H.; Grossman, J. C. Photoluminescent Arrays of Nanopatterned Monolayer  
32 MoS<sub>2</sub>. **2017**, 27, 1703688, 1–12.  
33  
34  
35  
36  
37  
38 (11) Zeng, Z.; Huang, X.; Yin, Z.; Li, H.; Chen, Y.; Li, H.; Zhang, Q.; Ma, J.; Boey, F.; Zhang,  
39 H. Fabrication of Graphene Nanomesh by Using an Anodic Aluminum Oxide Membrane  
40 as a Template. *Adv. Mater.* **2012**, 24, 4138–4142.  
41  
42  
43  
44  
45  
46 (12) Su, S.; Zhou, Q.; Zeng, Z.; Hu, D.; Wang, X.; Jin, M.; Gao, X.; Notzel, R.; Zhou, G.;  
47 Zhang, Z.; Liu, J. Ultrathin Alumina Mask-Assisted Nanopore Patterning on Monolayer  
48 MoS<sub>2</sub> for Highly Catalytic Efficiency in Hydrogen Evolution Reaction. *ACS Appl. Mater.*  
49 *Interfaces.* **2018**, 10, 8026-8035.  
50  
51  
52  
53  
54  
55  
56  
57  
58  
59  
60

- 1  
2  
3  
4 (13) Fissell, W. H.; Dubnisheva, A.; Eldridge, A. N.; Fleischman, A. J.; Zydney, A. L.; Roy, S.  
5  
6 High-Performance Silicon Nanopore Hemofiltration Membranes. *J. Memb. Sci.* **2009**, *326*,  
7  
8 58–63.  
9  
10  
11  
12 (14) Striemer, C. C.; Gaborski, T. R.; McGrath, J. L.; Fauchet, P. M. Charge- and Size-Based  
13  
14 Separation of Macromolecules Using Ultrathin Silicon Membranes. *Nature* **2007**, *445*,  
15  
16 749–753.  
17  
18  
19  
20 (15) Patil, J. J.; Smith, B. D.; Grossman, J. C. Ultra-High Aspect Ratio Functional Nanoporous  
21  
22 Silicon via Nucleated Catalysts. *RSC Adv.* **2017**, *7*, 11537-11542.  
23  
24  
25 (16) Huang, Z.; Geyer, N.; Werner, P.; de Boor, J.; Gösele, U. Metal-Assisted Chemical  
26  
27 Etching of Silicon: A Review. *Adv. Mater.* **2011**, *23*, 285–308.  
28  
29  
30  
31 (17) Zhou, H.; Yu, F.; Liu, Y.; Zou, X.; Cong, C.; Qiu, C.; Yu, T.; Yan Z.; Shen X.; Sun L.;  
32  
33 Yakobson B. I.; Tour J. M. Thickness-Dependent Patterning of MoS<sub>2</sub> Sheets with Well-  
34  
35 Oriented Triangular Pits by Heating in Air. *Nano Res.* **2013**, *6*, 703–711.  
36  
37  
38  
39 (18) Yamamoto, M.; Einstein, T. L.; Fuhrer, M. S.; Cullen, W. G. Anisotropic Etching of  
40  
41 Atomically Thin MoS<sub>2</sub>. *J. Phys. Chem. C* **2013**, *117*, 25643-25649.  
42  
43  
44 (19) Wu, J.; Li, H.; Yin, Z.; Li, H.; Liu, J.; Cao, X.; Zhang, Q.; Zhang H. Layer Thinning and  
45  
46 Etching of Mechanically Exfoliated MoS<sub>2</sub> Nanosheets by Thermal Annealing in Air.  
47  
48 *Small* **2013**, *9*, 3314–3319.  
49  
50  
51 (20) Oh, H. M.; Han, G. H.; Kim, H.; Bae, J. J.; Jeong, M. S.; Lee, Y. H. Photochemical  
52  
53 Reaction in Monolayer MoS<sub>2</sub> via Correlated Photoluminescence, Raman Spectroscopy,  
54  
55  
56  
57  
58  
59  
60

- 1  
2  
3  
4 and Atomic Force Microscopy. *ACS Nano* **2016**, *10*, 5230-5236.  
5  
6  
7 (21) Wei, X.; Yu, Z.; Hu, F.; Cheng, Y.; Yu, L.; Wang, X.; Xiao, M.; Wang, J.; Wang, X.; Shi,  
8 Y. Mo-O Bond Doping and Related-Defect Assisted Enhancement of Photoluminescence  
9 in Monolayer MoS<sub>2</sub>. *AIP Advances* **2014**, *4*, 123004.  
10  
11  
12  
13  
14  
15 (22) Nan, H.; Wang, Z.; Wang, W.; Liang, Z.; Lu, Y.; Chen, Q.; He, D.; Tan, P.; Miao, F.;  
16 Wang, X.; Wang J.; Ni Z. Strong Photoluminescence Enhancement of MoS<sub>2</sub> through  
17 Defect Engineering and Oxygen Bonding. *ACS Nano* **2014**, *8*, 5738–5745.  
18  
19  
20  
21  
22  
23 (23) Mouri, S.; Miyauchi, Y.; Matsuda, K. Tunable Photoluminescence of Monolayer MoS<sub>2</sub>  
24 via Chemical Doping. *Nano Lett.* **2013**, *13*, 5944-5948.  
25  
26  
27  
28 (24) Chakraborty B.; Bera A.; Muthu D. V. S.; Bhowmick, S.; Waghmare, U. V; Sood, A. K.  
29 Symmetry-Dependent Phonon Renormalization in Monolayer MoS<sub>2</sub> Transistor. *Phys. Rev.*  
30 *B* **2012**, *85*, 161403.  
31  
32  
33  
34  
35  
36 (25) Splendiani, A.; Sun, L.; Zhang, Y.; Li, T.; Kim, J.; Chim, C. -Y.; Galli, G.; Wang, F.  
37 Emerging Photoluminescence in Monolayer MoS<sub>2</sub>. *Nano Lett.* **2010**, *10*, 1271–1275.  
38  
39  
40  
41 (26) Wang, S.; Rong, Y.; Fan, Y.; Pacios, M.; Bhaskaran, H.; He, K.; Warner, J. H. Shape  
42 Evolution of Monolayer MoS<sub>2</sub> Crystals Grown by Chemical Vapor Deposition. *Chem.*  
43 *Mater.* **2014**, *26*, 6371–6379.  
44  
45  
46  
47  
48  
49 (27) Wang, S.; Weil, B.D.; Li, Y.; Wang, K.X.; Garnett, E.; Fan, S.; Cui, Y. Large-Area Free-  
50 Standing Ultrathin Single-Crystal Silicon as Processable Materials. *Nano Lett.* **2013**, *13*,  
51 4393-4398.  
52  
53  
54  
55  
56  
57  
58  
59  
60

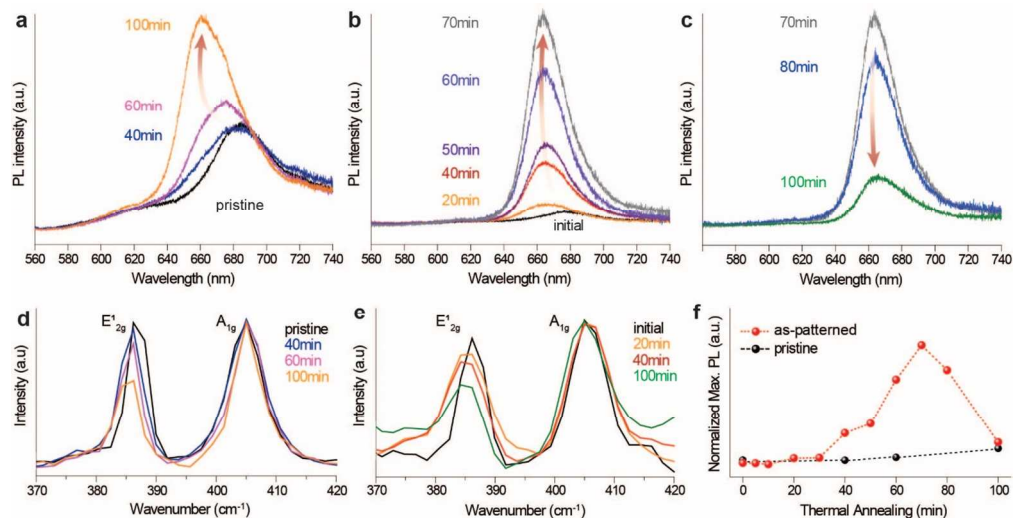
**For Table of Contents Only**





Effect of thermal annealing on the morphology of nanoporous  $\text{MoS}_2$ . (a) SEM image of a  $\text{MoS}_2$  domain after initial 2 min  $\text{O}_2$  plasma treatment through a 50 nm-thick NPSi mask. (b) SEM image of the  $\text{MoS}_2$  domain in (a) after 30 min of thermal annealing in air. (c) SEM image of a  $\text{MoS}_2$  domain from an identical sample after 60 min of annealing. (d) SEM image of a  $\text{MoS}_2$  domain from an identical sample after 100 min of annealing. (e) Magnified view of the sample in (a) showing individual pores with diameter  $\sim 70$  nm. (f) Magnified view of the sample in (b) showing nano-patterns of enlarged pores produced in the monolayer  $\text{MoS}_2$ . (g) Magnified view of the sample in (c) showing further expanded and converged pores. (h) Magnified view of the sample in (d) showing  $\text{MoS}_2$  flakes and oxidized  $\text{MoS}_2$  particles. (i) Plot of  $\text{MoS}_2$  edge density and porosity with respect to thermal annealing time for  $\text{O}_2$  plasma etched samples.  $N=3$  for all data. (j) SEM image of a  $\text{MoS}_2$  domain located half on a 50 nm thick NPSi etch mask and half on non-porous silicon after  $\text{O}_2$  plasma treatment and 60 min of thermal annealing. (k) SEM image of a pristine  $\text{MoS}_2$  domain after 100 min of thermal annealing in air.

167x160mm (220 x 220 DPI)



165x85mm (220 x 220 DPI)